





Modeling of Barrier Breaching During Hurricanes Sandy and Matthew

Christie A. Hegermiller¹ , John C. Warner¹ , Maitane Olabarrieta² ,
Christopher R. Sherwood¹ , and Tarandeep S. Kalra³

¹U.S. Geological Survey, Woods Hole Coastal and Marine Science Center, Woods Hole, MA, USA, ²Engineering School of Sustainable Infrastructure and Environment (ESSIE), University of Florida, Gainesville, FL, USA, ³Integrated Statistics, U.S. Geological Survey, Woods Hole, MA, USA

Key Points:

- The Coupled Ocean-Atmosphere-Wave-Sediment Transport model was adapted to include infragravity wave dynamics and applied to investigate barrier breaching during two hurricanes
- Different breaching mechanisms driven by remote to local forcing led to barrier breaches modeled with good skill
- Ocean-side processes were as important as back-barrier processes when breaching occurred from back-barrier inundation, and vice-versa

Supporting Information:

Supporting Information may be found in the online version of this article.

Correspondence to:

C. A. Hegermiller,
chehermiller@usgs.gov

Citation:

Hegermiller, C. A., Warner, J. C., Olabarrieta, M., Sherwood, C. R., & Kalra, T. S. (2022). Modeling of barrier breaching during Hurricanes Sandy and Matthew. *Journal of Geophysical Research: Earth Surface*, 127, e2021JF006307. <https://doi.org/10.1029/2021JF006307>

Received 9 JUN 2021

Accepted 16 JAN 2022

Abstract Physical processes driving barrier island change during storms are important to understand to mitigate coastal hazards and to evaluate conceptual models for barrier evolution. Spatial variations in barrier island topography, landcover characteristics, and nearshore and back-barrier hydrodynamics can yield complex morphological change that requires models of increasing resolution and physical complexity to predict. Using the Coupled Ocean-Atmosphere-Wave-Sediment Transport (COAWST) modeling system, we investigated two barrier island breaches that occurred on Fire Island, NY during Hurricane Sandy (2012) and at Matanzas, FL during Hurricane Matthew (2016). The model employed a recently implemented infragravity (IG) wave driver to represent the important effects of IG waves on nearshore water levels and sediment transport. The model simulated breaching and other changes with good skill at both locations, resolving differences in the processes and evolution. The breach simulated at Fire Island was 250 m west of the observed breach, whereas the breach simulated at Matanzas was within 100 m of the observed breach. Implementation of the vegetation module of COAWST to allow three-dimensional drag over dune vegetation at Fire Island improved model skill by decreasing flows across the back-barrier, as opposed to varying bottom roughness that did not positively alter model response. Analysis of breach processes at Matanzas indicated that both far-field and local hydrodynamics influenced breach creation and evolution, including remotely generated waves and surge, but also surge propagation through back-barrier waterways. This work underscores the importance of resolving the complexity of nearshore and back-barrier systems when predicting barrier island change during extreme events.

Plain Language Summary Barrier islands are particularly vulnerable to coastal erosion and flooding during extreme storms, such as hurricanes, because they are narrow and low-lying. Breaching across a barrier, when the ocean becomes connected to a back-barrier waterway, can result in damage to coastal communities requiring extensive repair efforts, and changes to ocean navigation or water dynamics that sometimes persist for many years. Barrier breaching can be driven by both ocean and back-barrier waterway processes. However, the conceptual framework describing coastal change during an extreme storm often only considers ocean processes. In this work, we hindcast barrier breaching using a physics-based numerical model that was recently extended to include infragravity (IG) waves. IG waves are long waves with periods of 25 s to 5 min, which contribute substantially to extreme water levels during hurricanes. The model was able to predict breach formation with good skill, though the modeled breaches did not occur in the exact locations where breaches were observed. Through analyses of modeled water levels, waves, and sand movement, this work demonstrates the importance of resolving the co-evolution of the beach, the ocean, and the back-barrier.

1. Introduction

Morphological changes to barrier islands have long been understood and evaluated within the context of the Sallenger (2000) storm impact scale, which identifies regimes of storm-induced changes based on comparison of total water levels to the elevations of the dune toe and dune crest. Significant morphological changes to the nearshore, beach face and berm, dune, and back-barrier occur as ocean water levels increase through swash, collision, overwash, and inundation regimes (Sallenger, 2000). During collision, sediment is eroded from the dune toe and beach face and transported offshore, often accumulating in shore-parallel nearshore bars. During overwash and inundation, sediment transport is primarily directed toward the back-barrier, creating washover fans that are critical to barrier island evolution over long time scales (decades to millennia; Donnelly et al., 2006). Modifications to barrier island topography during hurricanes, for example, breaching, can influence flooding dynamics

and post-storm beach recovery, as both water and sediment are exchanged between back-barrier waterways, the nearshore, and the inner shelf (e.g., Cañizares & Irish, 2008; Defne et al., 2019; Gharagozlou et al., 2021; Miselis et al., 2016).

Barrier island breaching can occur from inundation from either the ocean toward the back-barrier, or vice-versa. Several recent studies have discussed the importance of the ocean-back-barrier water level gradient in modulating the direction of overwash, inundation, and inlet currents (Coogan et al., 2019; Engelstad et al., 2017; Harter & Figlus, 2017; Passeri et al., 2018; Safak et al., 2016; Sherwood et al., 2014; Smallegan & Irish, 2017). The hydrodynamic processes that drive elevated ocean water levels include tides, sea level pressure (SLP)-driven inverse barometer effect, baroclinic effects (Pringle et al., 2019), wind-driven storm surge and wave run-up. Wave run-up consists of a time-averaged component (wave setup) and an oscillatory component (swash). Swash is driven by both sea-swell (SS; 0.04–1 Hz) and infragravity (IG; 0.003–0.04 Hz) wave motions. Water levels may become elevated in the back-barrier with respect to the ocean as the result of a wide range of processes, including tide and surge phase lags, wave-driven fluxes of water into the back-barrier, runoff from upland precipitation, and varied response to atmospheric forcing between the back-barrier and ocean, for example, wind-driven setup along the back-barrier and setdown in the ocean (Goff et al., 2010, 2019; Harter & Figlus, 2017; Sherwood et al., 2014). Extension of the Sallenger (2000) scale to include a regime dominated by seaward flow and sediment transport (“storm-surge ebb,” Goff et al., 2010; or “outwash,” Over et al., 2021) allows for further resolution of processes that govern long-term barrier island migration. Barriers with large back-barrier bays susceptible to wind-driven surge have been recognized previously as sites where these processes can be important.

Observations of hydrodynamics relevant to barrier island breaching during extreme events are often limited to long-term deployments of wave buoys (e.g., National Data Buoy Center [NDBC]; ndbc.noaa.gov) and water level gages (e.g., National Oceanic and Atmospheric Administration [NOAA]; tidesandcurrents.noaa.gov), though rapid deployments of pressure sensors in response to incoming storm forecasts are increasingly prioritized (e.g., McCallum et al., 2013). Efforts to observe nearshore hydrodynamics in situ are often limited to a single transect in the cross-shore (Engelstad et al., 2017; Sherwood et al., 2014). Large-scale deployments including multiple cross-shore transects (e.g., Coogan et al., 2019) illustrate that substantial alongshore variability in nearshore hydro- and morphodynamics can occur over small spatial scales during extreme events. Observations of active sediment transport or time-varying morphological changes are further limited. Lidar and photogrammetry techniques have allowed for rapid assessment of morphological changes following a storm, which integrates landward- and seaward-directed transport in time (Sherwood et al., 2018). Thus, linkage between the observed hydrodynamic conditions and the time series of morphological change remains difficult. Physics-based numerical modeling can effectively bridge this gap, and the state of morphodynamic modeling for these types of applications was recently reviewed in Sherwood et al. (2021).

XBeach-Surfbeat (D. Roelvink et al., 2009) has often been used for 1D profile and 2D spatial morphological simulations of the nearshore, beach, and dune during storms. Studies have illuminated the mechanisms responsible for profile change in the swash, collision, overwash, and inundation regimes of the Sallenger (2000) storm impact scale (e.g., Sherwood et al., 2014; Splinter & Palmsten, 2012) and have identified the primary drivers of alongshore variability in morphological change (e.g., De Vet et al., 2015; de Winter et al., 2015; Harter & Figlus, 2017; Passeri et al., 2018; Thiel de Vries et al., 2011). Extensive application and calibration of XBeach-Surfbeat has revealed sensitivity to a few key parameterizations representing processes that are either not fully understood or not resolvable due to, for example, model horizontal resolution or the wave group approach (Callaghan et al., 2013; De Vet et al., 2015; Elsayed & Oumeraci, 2017; Kalligeris et al., 2020; McCall et al., 2010; Passeri et al., 2018; Rafati et al., 2021; Schweiger et al., 2020; Simmons et al., 2019; van der Lugt et al., 2019; Vousdoukas et al., 2012). XBeach, however, parameterizes cross-shore transport in a depth-averaged approach. Further, XBeach-Surfbeat in transect applications does not resolve alongshore variations in hydro- or morphodynamics, which are necessary to accurately reproduce observed alongshore variations in time-integrated morphological change (de Winter et al., 2015; Kalligeris et al., 2020; Thiel de Vries et al., 2011).

In this work, we present an analysis of barrier breaching using a modeling system that resolves three-dimensional variability in the nearshore processes and sediment transport. As part of a collaborative effort to advance event-based morphological modeling, a recent study by van der Lugt et al. (2019) used XBeach-Surfbeat in 2D spatial mode to explore morphodynamics of the same events investigated in the present study. The authors simulated breaching with high skill and quantified sensitivity of morphological change to uncertainty in hydrodynamic

forcing, such as wave height, ocean surge water level, and back-barrier water levels. As in other XBeach-Surfbeat studies, van der Lugt et al. (2019) found morphological change was highly sensitive to coefficients that modify wave-driven onshore sediment transport and bottom roughness variations with vegetation. As the present investigation applies a new model to breach morphodynamics, we also analyzed sensitivity of modeled morphological change to vegetation, implemented via two methods, one of which is similar to that used in van der Lugt et al. (2019). We further explored sensitivity to hydrodynamic forcing by quantifying the impact of IG waves on morphological change. We investigated the hydro- and morphodynamic processes that created breaches on two barrier islands: Fire Island, NY during Hurricane Sandy (2012) and near Matanzas, FL during Hurricane Matthew (2016). These events were chosen because they represent significant breaching events for which adequate elevation data are available before and after the storms and for which high-fidelity meteorological hindcasts were developed by the Naval Research Laboratory. This paper is organized as follows: Sections 2 and 3 discuss characteristics of Hurricanes Sandy and Matthew, respectively, and the breaches created during those events, within the context of their coastal environments. Section 4 reviews the methodology, including the hydrodynamic, SS wave, IG wave, and morphodynamic modeling components. Section 5 assesses the skill of the hydrodynamic and wave models using water level and wave observations. We compare observed and modeled morphological change and discuss model sensitivity for Fire Island in Section 6. We analyze the processes that created the breach at Matanzas in Section 7. Brief concluding remarks are found in Section 8.

2. Hurricane Sandy and Breaching at Fire Island, NY

Hurricane Sandy was a Saffir-Simpson Category 2 hurricane that impacted the US East Coast in late October 2012 (Figure 1). Sandy transited the Western Atlantic Ocean relatively far offshore for 5 days until turning west to make landfall in New Jersey on 29 October 2012, causing extreme coastal erosion and flooding (Hapke et al., 2013) with destruction to residences and infrastructure along the East coast, particularly in the New York Bight (NYB). Maximum winds were ~ 50 m/s, minimum SLP recorded was 940 mbar (HURDAT2; Landsea & Franklin, 2013), maximum observed wave heights were ~ 9.5 m at NDBC wave buoy 44025 in 36 m water depth, and storm surge was 3.5 m at the Battery (NOAA Tides and Currents). A thorough description of Hurricane Sandy and exploration of the storm-driven morphological changes of shoreface connected sand ridges on the inner shelf of Long Island, NY can be found in Warner et al. (2017).

During Sandy, barrier island breaching occurred at the site of a historical breach on an uninhabited section of Fire Island, NY. Fire Island is a ~ 40 km long, 0.25–0.9 km wide barrier island (Figures 2a–2c). This “Wilderness Breach” remains open, with active tidal flow between Great South Bay and the Atlantic Ocean. Significant research efforts have characterized the erosion, breaching, and recovery of Fire Island from post-storm topographic, bathymetric, and sediment observations and modeling efforts (e.g., Hapke et al., 2013; van der Lugt et al., 2019; Van Ormondt et al., 2020). Pre- (May 2012; Fredericks et al., 2016) and post-storm (5 November 2012; Stockdon et al., 2013) LiDAR surveys provided topographic data for model initialization and comparison. Reported horizontal and vertical accuracies were 0.194 and 0.147 m, respectively, for LiDAR surveys (Stockdon et al., 2013). Offshore and back-barrier bathymetry was supplemented by National Centers for Environmental Information (NCEI) Continuously Updated Digital Elevation Model (CUDEM). All elevations are referenced to the North American Vertical Datum of 1988 (NAVD88).

3. Hurricane Matthew and Breaching at Matanzas, FL

Hurricane Matthew was a Saffir-Simpson Category 5 hurricane that impacted the Caribbean Islands and US East Coast in early October 2016 (Figure 1). The hurricane paralleled the South Atlantic Bight (SAB) coastline within 50 km for 2 days until landfall in South Carolina on 8 October 2016. Extensive flooding and coastal erosion due to extreme storm surge, waves, and rainfall were experienced in the SAB during Matthew's close transit (HURDAT2; Landsea & Franklin, 2013; Sherwood et al., 2018). Maximum wind speeds were ~ 75 m/s, maximum observed wave heights were ~ 8 m at NDBC wave buoy 41009 in ~ 40 m water depth (ndbc.noaa.gov), and maximum storm surge was reported to be ~ 3 m in parts of Florida. A description of Hurricane Matthew's evolution through the SAB, and an investigation of the role of the Gulf Stream in modulating wave heights and water levels during this hurricane can be found in Hegermiller et al. (2019).

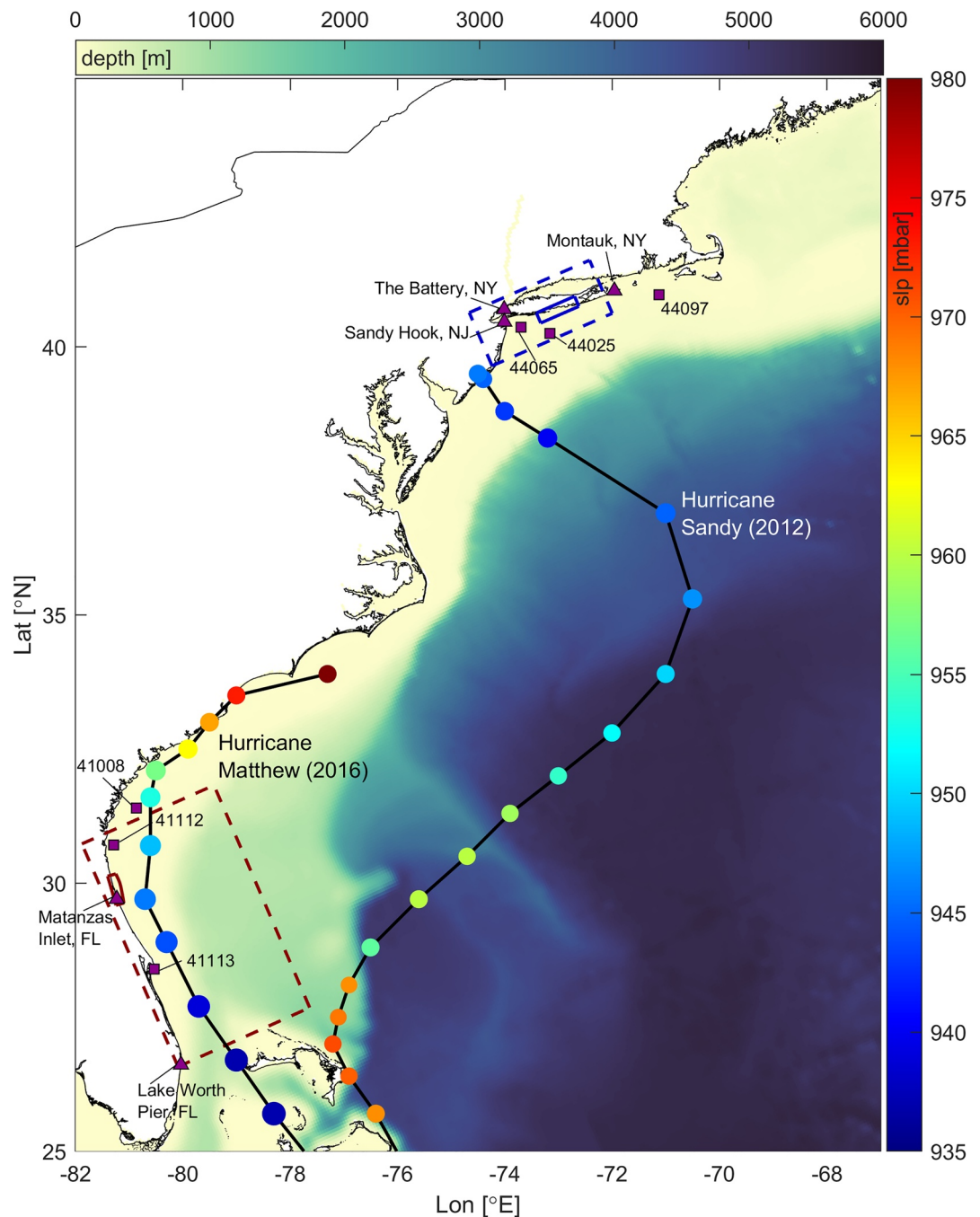


Figure 1. Storm track (black lines) and intensities (minimum sea level pressure; colored dots) for Hurricanes Sandy and Matthew. The largest, lowest resolution model domain extends beyond the limits of the figure to encompass the western North Atlantic Ocean. Magenta triangles and squares indicate water level gages and wave buoys, respectively, used for comparison in the supplemental material. Regional (~1 km) and sub-regional (~200 m) model domains for the Hurricane Sandy simulations are shown in the dashed and solid blue boxes, and for the Hurricane Matthew simulations are shown in the dashed and solid red boxes.

Breaching of a small barrier separating the ocean from the Intracoastal Waterway south of Matanzas, FL occurred on 7 October 2016 (Figures 2d–2f). The barrier is 1.7 km long and less than 0.15 km wide, characterized by a sandy beach with houses and a paved road running along parts of the dune crest. The Intracoastal Waterway is populated by wetland vegetation and mangroves. The breach location is 2 km south of Matanzas Inlet (Figure 2d), through which the tide propagates to the Intracoastal Waterway. Pre-storm topo-bathymetric LiDAR (June 2015;

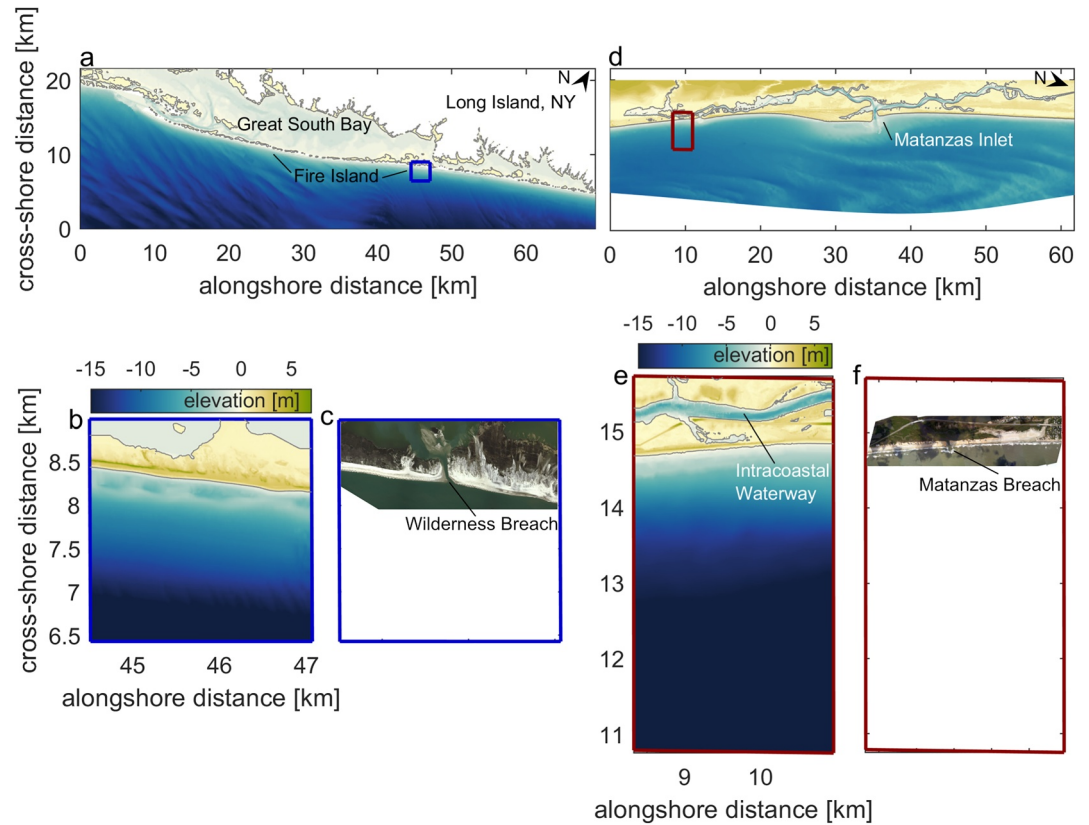


Figure 2. (a) The sub-regional model domain encompassed Great South Bay and the Atlantic Ocean offshore of Fire Island, NY. A local domain (blue box) resolved hydro- and morphodynamic processes over a small section of Fire Island during Hurricane Sandy. (b) Inset of the local domain and pre-Sandy bathymetry and topography. (c) Inset of the local domain and post-Sandy National Oceanic and Atmospheric Administration (NOAA), National Ocean Service, National Geodetic Survey (2013) Emergency Response Imagery (ERI) showing Wilderness Breach. (d) The sub-regional model domain encompassed the Intracoastal Waterway, Matanzas Inlet, and Atlantic Ocean offshore of Matanzas, FL and local domain (red box) over the barrier during Hurricane Matthew. (e) Inset of the local domain and pre-Matthew bathymetry and topography. (f) Inset of the local domain and post-Matthew NOAA ERI showing Matanzas Breach.

JALBTCX, 2016) and post-storm topo-bathymetric LiDAR (November 2016; JALBTCX, 2017) and topography from 4D structure from motion from oblique aerial imagery (8 October 2016; Sherwood et al., 2018) were available to capture hurricane-driven morphological changes. Reported vertical accuracy for topographic data was 0.095 m and for bathymetric data was 0.125 m. Offshore and Intracoastal Waterway LiDAR-derived bathymetry were supplemented by the NCEI CUDEM. Elevations are referenced to NAVD88.

4. Model Setup

The Coupled Ocean-Atmosphere-Wave-Sediment Transport modeling system (COAWST; Warner et al., 2008, 2010, 2019) was used to explore breaching at Fire Island and Matanzas during Hurricanes Sandy and Matthew. For each storm, a suite of model grids with increasing horizontal resolutions represented the ocean basin, regional, sub-regional, and local scales. At the ocean basin, regional, and sub-regional scales, the Regional Ocean Modeling System (ROMS; version 3.8) and Simulating Waves Nearshore model (SWAN; version 41.31) were two-way coupled and forced with one-way coupling by an atmospheric reanalysis using the Coupled Ocean Atmosphere Mesoscale Prediction System-Tropical Cyclone (COAMPS-TC). At the local scale, ROMS, an IG wave driver (InWave), and the Community Sediment Transport Modeling System (CSTMS) were coupled. COAWST has been used extensively to simulate hurricane atmospheric conditions, oceanic response, wave fields, and sediment dynamics. The reader is referred to Warner et al. (2017) and Hegermiller et al. (2019), which explored aspects of Hurricanes Sandy and Matthew, respectively.

4.1. Ocean Model

ROMS is a three-dimensional, free surface, terrain-following hydrodynamic model that solves finite differences approximations of the Reynolds-Averaged Navier Stokes equations on an Arakawa C grid assuming hydrostatic equilibrium and Boussinesq approximations (Haidvogel et al., 2000, 2008; Shchepetkin & McWilliams, 2005; Warner et al., 2008). For each hurricane, a suite of nested grids telescoped from the ocean basin scale to the sub-regional scale (Figure 1). For Hurricane Sandy, simulations were performed for 25–30 October 2012 on a curvilinear grid extending over the US East and Gulf (USE) coasts at ~5 km horizontal resolution, a regional NYB grid at ~700 m resolution, and a sub-regional grid at ~100–200 m resolution, with 16 terrain-following vertical layers. For Hurricane Matthew, simulations were performed for 1–9 October 2016 over the USE grid, a regional SAB grid at ~1 km horizontal resolution, and a sub-regional grid at ~100–200 m resolution, with 16 terrain-following vertical layers. The sub-regional domains resolved interactions between tides, wind and SLP-driven surge, and wave dynamics in coastal and back-barrier waters (Figure 2). Further details on model implementation, including boundary conditions, time stepping, turbulence closures, and advection and mixing schemes, can be found in Warner et al. (2017) and Hegermiller et al. (2019).

Bulk wave parameters from SWAN, described below, were exchanged with ROMS every 15 min to account for wave contribution to the circulation through the vortex force formalism (Kumar et al., 2012; Uchiyama et al., 2010), which includes the transfer of momentum from waves to currents, Stokes flows, and turbulence injected into the surface ocean via wave breaking. Wave rollers were also generated from wave breaking and were dissipated following Reniers et al. (2004). Half of the energy dissipated during breaking was used in the generation of rollers.

4.2. Wave Model

SWAN is a third-generation spectral wave model that solves the evolution of wave action through wave propagation, shoaling, and refraction over bathymetry and currents, wind wave growth, dissipation due to whitecapping, bottom friction, and depth-limited breaking, and nonlinear triad and quadruplet wave-wave interactions (Booij et al., 1999). SWAN simulations were performed over the same nested grids used for ROMS. Wave spectra were resolved with 6° directional resolution and 24 frequency bins ranging logarithmically from 0.04 to 1 Hz. SWAN was implemented with default formulations for wind-wave growth, dissipation due to whitecapping, and dissipation due to bottom friction. Spectral redistribution of energy by nonlinear quadruplet wave-wave interactions was calculated using the discrete interaction approximation. An implicit, first order, backward space, backward time marching scheme was used to solve the wave action balance equation. SWAN was initialized with a stationary computation for the wind fields at the beginning of the simulations. ROMS exchanged current velocities and water levels with SWAN to resolve wave-current interaction and the enhancement or reduction of depth-limited breaking and bottom friction with tidal fluctuations or storm surge.

4.3. Atmospheric Forcing

COAWST simulations were forced by COAMPS-TC atmospheric fields reanalyzed to best capture the hurricane track, minimum SLP, and radius of maximum winds (Doyle et al., 2014). Atmospheric forcing included longwave and shortwave radiation, SLP, wind velocity at 10 m above the ocean surface, precipitation rate, air temperature, and relative humidity at 4 km horizontal resolution and 3-hr temporal resolution. Air-sea heat, fresh-water, and momentum fluxes were calculated following COARE 3.0 parameterizations (Fairall et al., 1996, 2003), with inclusion of surface wave roughness following Taylor and Yelland (2001) and a limit on the roughness length following Davis et al. (2008).

4.4. Infragravity Wave Driver and Sediment Transport Formulations

ROMS and CSTMS (Warner et al., 2008) were two-way coupled with an IG wave driver (InWave; Olabarrieta et al., in prep) at the local scale to resolve nearshore hydro- and morphodynamics (Figure 2, Text S1 in Supporting Information S1). InWave is a phase-averaged, group-resolving numerical model that functions like XBeach-Surfbeat, in which wave groups are generated statistically from frequency directional SS wave spectra at the offshore boundary of the domain. InWave resolves the SS waves with a characteristic frequency and

full directional resolution using the wave-action balance equation, which accounts for refraction and shoaling, wave-current interaction, and energy dissipation due to wave breaking and bottom friction. InWave accounts for wave group variations of SS wave action density, causing wave forces and breaking to vary at the wave group scale. Consequently, hydrodynamic forces varying at the wave group scale can create variations in sediment transport at these scales as well. IG waves bound to the wave groups are solved analytically following Van Dongeren et al. (2003) and imposed on the offshore ROMS boundary as variations in the free surface and currents. IG waves driven by breakpoint forcing are generated within the domain as stress is exerted from breaking wave groups (J. A. Roelvink, 1993) to surfzone currents via the vortex force formalism (Kumar et al., 2012). The primary equations solved in InWave are detailed in Text S1 in Supporting Information S1.

The local-scale ROMS and InWave domains were oriented orthogonal to the coastlines and extended from the 20-m depth contour to the back-barrier, and alongshore for several kilometers (Figure 2). Horizontal resolution at Fire Island varied in the cross-shore from 2.5 m at the dune crest to 25 m offshore and, in the alongshore, was 5 m. Horizontal resolution at Matanzas varied in the cross-shore from <2 m at the dune crest to ~10 m offshore and toward the back-barrier. Horizontal resolution in the alongshore was 10 m. Alongshore resolution at Fire Island was higher than at Matanzas due to a priori expectation of the importance of small-scale dune crest variations in breach initiation (Hapke et al., 2013). Simulations at this scale were one-way nested into the sub-regional simulations described above and resolved hydro- and morphodynamics during the 24 hr around the peak of the storms. Initial and boundary conditions for free-surface elevations and barotropic velocities were interpolated from the sub-regional simulations on all open boundaries of the local domain, including those boundaries in back-barrier waterways. Note, this indicates that the simulations were not periodic in the alongshore. Frequency directional wave spectra from sub-regional ROMS/SWAN simulations output every 15 min at the center points of the offshore boundary of the local domains were used to force wave groups and bound IG wave generation. The models were run with seven vertical levels and a 0.1 s timestep for the baroclinic mode. Wetting and drying of grid cells was activated. Nesting from the ocean basin scale allowed for representation of relevant physical processes in the hydrodynamic forcing at the local scale, including tides, wind- and SLP-driven surge, wave setup, and other circulation features.

The CSTMS suite of sediment transport and morphodynamic formulations were used to simulate morphological changes in the nearshore, beach, dune, and back-barrier, including bar migration and washout, beach and dune face erosion, dune lowering, washover deposition, and channel scouring. The SANTOSS formulation (Van der A et al., 2013) for bedload transport under waves with velocity skewness and acceleration asymmetry was recently implemented in COAWST (Kalra et al., 2019). The nonlinear wave shapes are related to the Ursell number and sand transport over each portion of the wave cycle is calculated. In the COAWST implementation, two parameters α_w and α_c modify the relative magnitude of the bedload transport associated with wave-driven transport and current-driven transport, respectively. These parameters perform the same function that the coefficient fac_{ua} does (for both wave- and current-driven transport) in XBeach-Surfbeat, although the bedload transport formulations are different. van der Lugt et al. (2019) and Rafati et al. (2021) referred to the wide range of values for this parameter, indicating that these formulations may not physically represent the processes (e.g., wave shape). We used values of $\alpha_c = 0.65$ and $\alpha_w = 0.35$ that attenuate transport calculated by the published formulae and preferentially favor current-driven transport, but extensive calibration of these parameters is not within the scope of this work. Sediment slumping routines were implemented to account for avalanching at the wet-dry interface and underwater. Sediment slumping is governed by user-defined critical slopes for dry and wet sand, and dry and wet scaling parameters for the transport associated with this process. Model results were somewhat sensitive to these parameters, and they were adjusted to provide the best qualitative results for each case individually.

Lastly, landcover characteristics such as vegetation and infrastructure can affect sediment erosion, transport, and deposition from the dune crest (e.g., grasses, low bush, and paved surfaced) to the back-barrier waterways (e.g., mangroves and woody vegetation) and marsh platforms (Passeri et al., 2018; van der Lugt et al., 2019). Vegetation can influence morphodynamics by reducing sediment erosion, modifying transport, and increasing sediment deposition through compaction or stabilization of sediment by root masses and reduction in current velocities and modification of the vertical current structure. We implemented the effect of landcover on sediment erosion through three approaches (Table 1). *Method 1* used a spatially uniform, constant value of bed roughness length (z_0) = 0.0025 m. *Methods 2* and *3* incorporated variability of landcover classification derived from pre-storm National Agriculture Imagery Program (NAIP, 2018) images. A detailed explanation of the classification process

Table 1
Landcover Characteristics Were Classified Following van der Lugt et al. (2019; VDL19)

Manning's N	Method 1	Method 2	Method 3
VDL19	Uniform z_0 (m)	Varying z_0 (m)	Vegetation
0.02	0.0025	0.002	None
0.03	0.0025	0.02	None
0.045	0.0025	0.06	Height = 0.5 m Thickness = 0.01 m
0.05	0.0025	0.08	Height = 1.0 m Thickness = 0.05 m

Note. The effect on morphological change was explored through three methods: spatially uniform and constant bed roughness length (z_0), spatially varying z_0 , and implementation of the vegetation module of COAWST. For reference, we include the Manning's N for landcover classes used by VDL19.

can be found in van der Lugt et al. (2019). In *Method 2*, we implemented a spatially varying z_0 related to landcover type in pre-storm imagery. z_0 was translated from Manning's n guided by Smart (2004), assuming a water depth of 1 m. In *Method 3*, we activated the vegetation module within COAWST (Beudin et al., 2017; Kalra et al., 2017) to account for the effects of three-dimensional drag (momentum extraction) and enhanced vertical mixing on hydro- and morphodynamics. Vegetation properties, including diameter, stem density, height, and thickness, were related to landcover type in pre-storm imagery and guided by previous applications (Beudin et al., 2017). However, this is the first application of the vegetation module to subaerial vegetation. As a result, these values were somewhat arbitrary, but were selected to reflect the characteristics of the varied vegetation on barrier islands. For this proof of concept, plant diameter was uniform and constant at 0.03 m, and density at 10 stems/m², while height and thickness were varied. A scale factor was applied to the vegetation effects based on local bed elevation change versus plant height. If accretion occurred to the plant elevation or if the bed eroded to 0.5 m, the vegetation effects linearly diminished to zero, following van der Lugt et al. (2019). We explored sensitivity of the morphological change to landcover effects at Fire Island because the dunes and back-barrier marsh platform were vegetated (Figure 2c). We implemented *Method 1* and did not explore sensitivity to landcover effects at Matanzas because the barrier was primarily sandy (Figure 2f).

4.5. Morphological Change Assessment

Modeled morphological change was compared to observed morphological change derived from pre- and post-storm LiDAR surveys. We quantified model skill with mean bias, root-mean square error (RMSE), and Brier Skill Score (BSS) for four variables: bed elevation change, post-storm dune crest elevation, volume of sediment eroded, and volume of sediment deposited, all determined on cross-shore transects with spacing defined by the model grid. BSS was calculated as:

$$BSS = 1 - \frac{\frac{1}{N} \sum_{i=1}^N (y_i - x_i)^2}{\frac{1}{N} \sum_{i=1}^N (b_i - x_i)^2}$$

where x and y are observed and modeled variables, i is cross-shore transect 1: N , and b is the assumption of no morphological change (e.g., in the case of the variable bed elevation change, $b = 0$ (Sutherland et al., 2004)). Qualitative assessment of skill scores followed Table 11 in Sutherland et al. (2004). Statistics were calculated for the primary dunes on each barrier and excluded the back-barrier marsh platform and waterways.

5. Local Water Levels and Wave Heights

We assessed model skill for water levels and bulk wave parameters by comparing model output with observations at tide gages and offshore wave buoys (Text S2 and Figures S1–S4 in Supporting Information S1). RMSE ranged from 0.18 to 0.36 m in comparisons of water levels during Sandy and from 0.10 to 0.26 m during Matthew (Figures S1 and S3 in Supporting Information S1). RMSE of significant wave heights ranged from 0.57 to 1.04 m during Sandy and from 0.31 to 0.70 m during Matthew. The models generally overestimated peak water levels and wave heights during Sandy and slightly underestimated peak water levels and wave heights during Matthew (Figures S1 and S3 in Supporting Information S1). Overall, we concluded that the models reproduced the important water level and bulk wave characteristics with sufficient skill to provide accurate forcing for downscaled simulations of morphological changes.

During Sandy, wave conditions offshore of Fire Island grew from 3.5 to 8 m wave heights with peak wave periods growing from 11 to 17 s (Figure 3). Waves approached from the southeast then rotated to the southwest after the peak of the storm. Time series of water levels were output in the nearshore (purple dot in Figure 4d) at 2 Hz

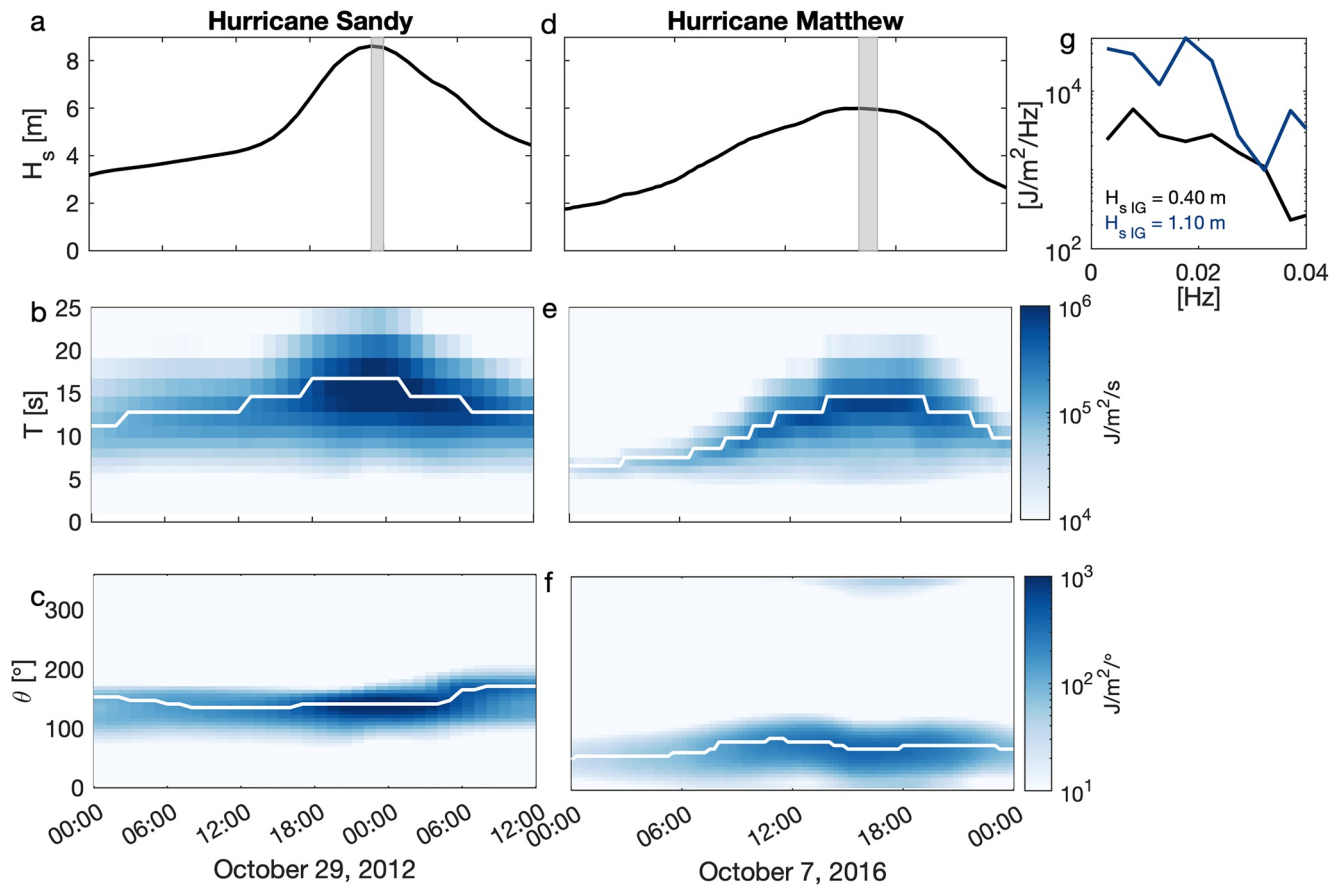


Figure 3. Imposed time series of (a and d) significant wave height (H_s), (b and e) frequency spectra, and (c and f) directional spectra for Hurricanes Sandy and Matthew. White lines on panels (b and e) are the peak wave period, and on panels (c and f) are the incident mean wave direction. (g) Infragravity wave energy spectrum at the peaks of Sandy (blue) and Matthew (black), indicated on panels (a and d) by the gray boxes, at the nearshore location indicated on Figures 4d and 6d.

for 1 hr and the energy spectrum at IG wave frequencies (frequency <0.04 Hz) was calculated. During peak SS energy, IG significant wave height was 1.10 m (Figure 3g).

Waves were less energetic offshore of Matanzas during Matthew, and grew from 2 to 6 m wave heights with peak wave periods of 14 s (Figure 3). Waves rotated from the east to the southeast during the storm and were nearly orthogonal to the beach during peak wave conditions. Time series analysis of modeled water levels output in the nearshore (purple dot in Figure 6d) indicate that during peak SS energy, IG significant wave height was 0.40 m.

6. Fire Island Breach

6.1. Morphological Change

Before Hurricane Sandy, the barrier island near the breach had continuous high dunes on the western end and broken, lower dunes backed by washover deposits on the eastern end (Figures 2b and 2c, 4a). After Sandy, beach, dune face, and dune crest erosion ($\sim 1\text{--}2$ m) were observed along the length of the barrier island (Figures 4b, 4c and 4m). The continuous, high dunes on the western end were eroded, but were less incised because overwash rarely overtopped these higher dune elevations and inundation did not exceed the dune crests. In contrast, on the eastern end, lower dune faces and crests were significantly eroded and overwash transported sand across the island and deposited it on the back-barrier. The breach developed at a narrow location in the barrier island, a historical breach location, and a local low spot in the dune crest (Figures 4b, 4c and 4m). Nearly 4 m of sediment were eroded at the breach location.

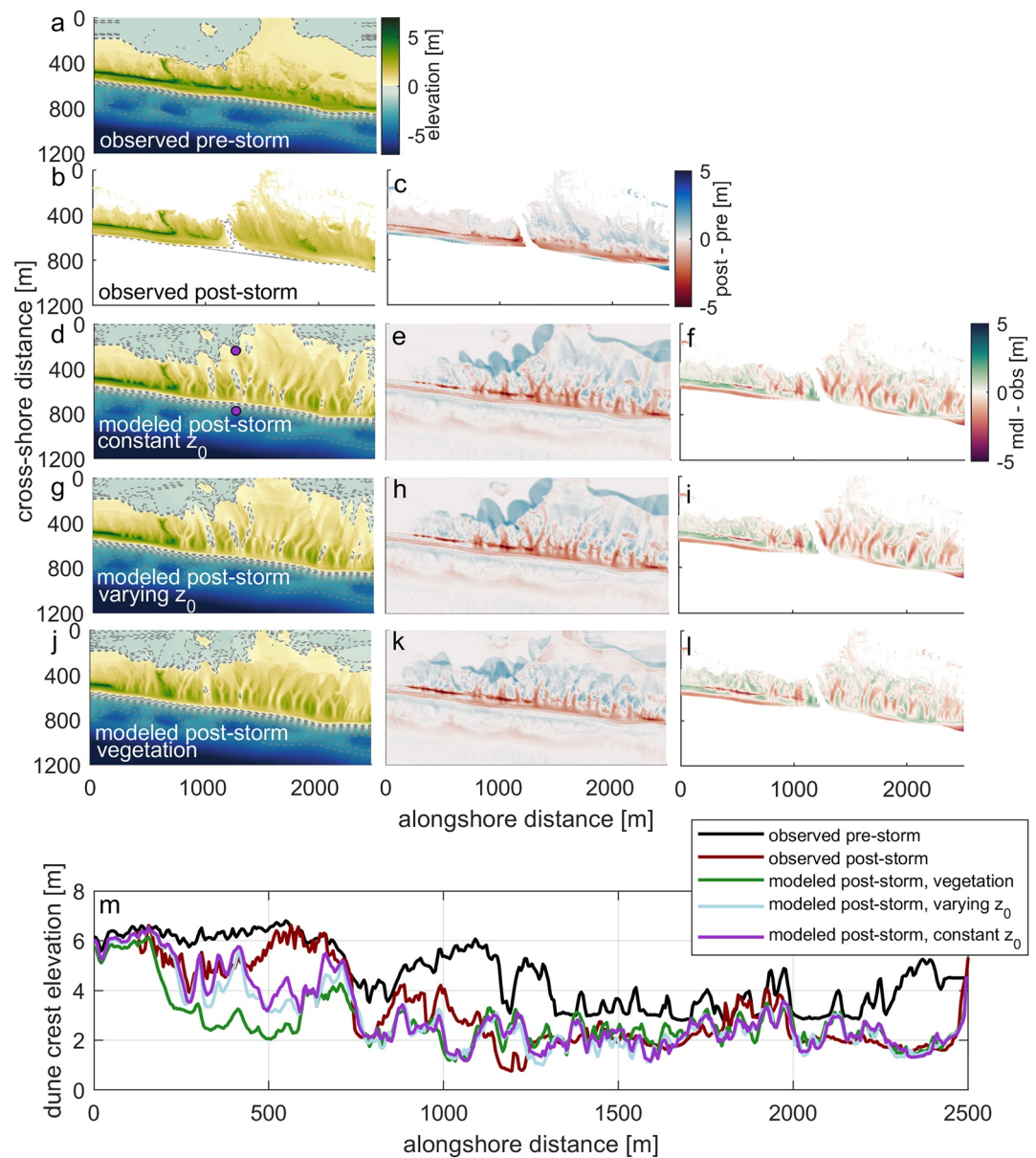


Figure 4. (a) Observed pre- and (b) post-storm and (d, g, j) modeled post-storm topography and bathymetry for Fire Island, NY after Hurricane Sandy. Contours indicate 0.4 m depth in 0.5 m increments. The two points in panel (d) indicate where water levels were extracted to calculate cross-barrier gradients. (c) Observed and (e, h, k) modeled change during the storm. (f, i, l) Difference (modeled – observed) in change. (m) Pre- and post-storm observed and modeled dune crest elevations.

Modeled change from the *Method 1* simulation (uniform, constant z_0) broadly reproduced observed morphological response to Sandy, including substantial dune and beach erosion, washover deposition, and breaching. Modeled change matched the spatial gradients in the observations. Dune erosion was predicted at the western end of the domain (Figures 4d, 4e and 4m), but the model also produced washover channels that cut the western dune crests and deposited sediment in the back-barrier, which was not observed. Additionally, the model predicted substantial dune crest lowering in locations where observations indicate that dune crests were preserved (Figure 4m: alongshore distance 500–800 m). On the eastern end, significant overwash was predicted. Modeled washover deposits were located further in the back-barrier than observed, indicating that modeled inundation may have been greater than what occurred or that “runaway” channelization occurred in the model, where lateral erosion of channel banks was limited by model resolution and channel scouring was exacerbated (Baar et al., 2019). Excess modeled inundation was likely driven by modeled wave heights, which overestimated observed wave heights by more

Table 2
Bias, Root Mean Square Error (RMSE), and Brier Skill Score (BSS) for Modeled Total Bed Elevation Change, Crest Elevation, Eroded Volume, and Deposited Volume Compared to Observations

		Fire Island, NY			Matanzas, FL	
		<i>Method 1</i>	<i>Method 2</i>	<i>Method 3</i>	<i>Baseline</i>	No IG waves
Total Change (m)	Bias	-0.11	-0.14	-0.01	-0.41	0.37
	RMSE	0.79	0.80	0.71	1.03	0.96
	BSS	0.48	0.46	0.59	0.08	0.21
Crest Elevation (m)	Bias	-0.27	-0.40	-0.56	-0.61	0.83
	RMSE	0.91	1.01	1.35	1.03	1.30
	BSS	0.72	0.65	0.37	0.38	0.01
Eroded Volume (m ³)	Bias	-116.73	-157.19	-64.41	-378.84	443.88
	RMSE	493.08	495.85	375.44	518.76	573.01
	BSS	0.45	0.44	0.68	0.23	0.06
Deposited Volume (m ³)	Bias	-19.84	-23.48	49.10	-83.73	-122.62
	RMSE	160.89	172.21	176.93	188.58	215.69
	BSS	0.49	0.41	0.38	0.27	0.04

than 1 m at nearby NDBC buoy 44025. The predicted breach was created ~250 m to the west of the observed breach (Figures 4f and 4m). The model overestimated total bed erosion, dune crest lowering, and volume eroded (Table 2). The model underestimated the volume deposited for the area of the primary dunes because washover deposits were predicted to extend further toward the back-barrier than observed and were outside of the area analyzed. The BSS for all variables indicated good model skill.

6.2. Sensitivity to Landcover Effects

We explored the sensitivity of the modeled morphological change to the effects of landcover classification, specifically vegetation. Modeled morphological change for the *Method 2* simulation (variable z_0) was characterized by increased erosion of the western dune crest compared to the *Method 1* simulation (Figure 4m). Model predictions deviated further from observations (Figures 4g–4i), with larger negative Bias, RMSE, and poorer skill across all variables (Table 2). Implementation of *Method 3* (vegetation module) resulted in improved overall predictions of bed elevation change, with a BSS of 0.59 (Table 2), despite increased erosion of the western dune crest relative to the other simulations (Figure 4m). The spatial extent of back-barrier deposition was greatly reduced, resulting in greater skill for eroded volume, but washover channelization across the dunes was similar to the other simulations (Figures 4e, 4k and 4l). Breaching occurred in the same location as *Method 1*.

Taken together, results suggest that the model performed well for erosion during the collision regime, but that morphological change during the overwash regime, particularly washover channelization in the back-barrier requires further study. Imposing spatially variable roughness resulted in poorer skill. Vegetation reduced flow across the back-barrier, but did not substantially hinder dune crest erosion or overwash. These sensitivity studies indicate that further development of the vegetation module to subaerial vegetation applications has potential to improve predictive skill of morphological models (Passeri et al., 2018; van der Lugt et al., 2019; Zheng et al., 2013).

6.3. Breaching Dynamics

We analyzed the hydrodynamics that drove breaching at Fire Island by extracting modeled water levels from a location in Great South Bay and a location at 2 m depth in the nearshore along the cross-barrier transect through the breach (Figures 4d and 5a). The sampling locations were separated by 470 m in the cross-shore. Note that the water-level time series in the nearshore is subject to setup by SS wave groups and water-level variations due to IG waves. We averaged these gradients over 30 min to remove wave fluctuations. Positive gradients indicate that ocean water levels were higher than back-barrier water levels, driving flow toward the back-barrier (Figure 5b).

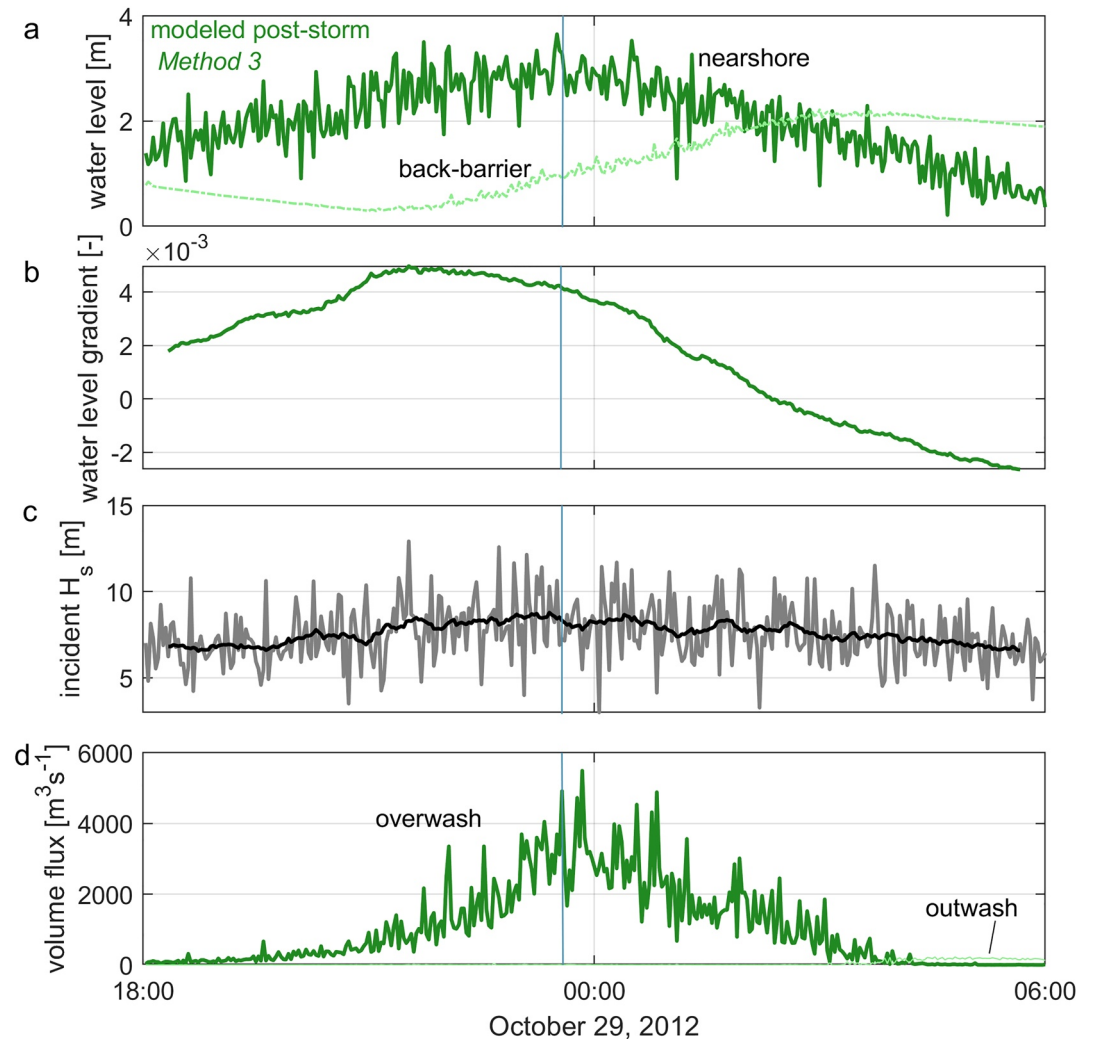


Figure 5. Time series of Hurricane Sandy (a) water levels in the nearshore (solid) and back-barrier (dashed) for the *Method 3* model simulation, (b) The cross-barrier water level gradient over ~ 470 m, averaged over individual wave groups, where negative indicates an offshore-directed water level gradient, (c) incident significant wave height (H_s) at the wave group scale (gray) and averaged (black). (d) Onshore (thick lines) and offshore (thin lines) volume flux over the dune crest integrated in the alongshore. Blue vertical lines indicate the approximate time of breaching.

Incident significant wave heights were extracted from the model at the offshore boundary and averaged over 30 min (Figure 5c). Onshore and offshore volume flux of water across the dune crest was calculated and integrated in the alongshore (Figure 5d).

As ocean storm surge and wave height increased in the early stages of the storm, the model suggests that back-barrier water levels were falling as tides ebbed in Great South Bay (Figure 5). Nearshore water levels were ~ 2 m, but wave heights were 7 m, and total water levels were likely sufficient for dune erosion in the collision regime. During low tide in the back-barrier, the water-level gradient across the barrier was at its maximum. However, dunes had not eroded enough for vulnerable low spots to experience inundation. Instead, modeled overwash increased with increasing nearshore water levels and wave conditions, which both peaked at high tide in the ocean. Substantial overwash occurred following maximum nearshore water levels and continued despite a weakening ocean-back-barrier water-level gradient, indicating that dunes were eroded and some locations were inundated. The water-level gradient approached zero and became negative as storm surge receded, ocean tides ebbed, and back-barrier water levels approached high tide. Model results suggest that this negative gradient drove weak flows through the breaches toward the ocean, causing further erosion of the new inlet channels.

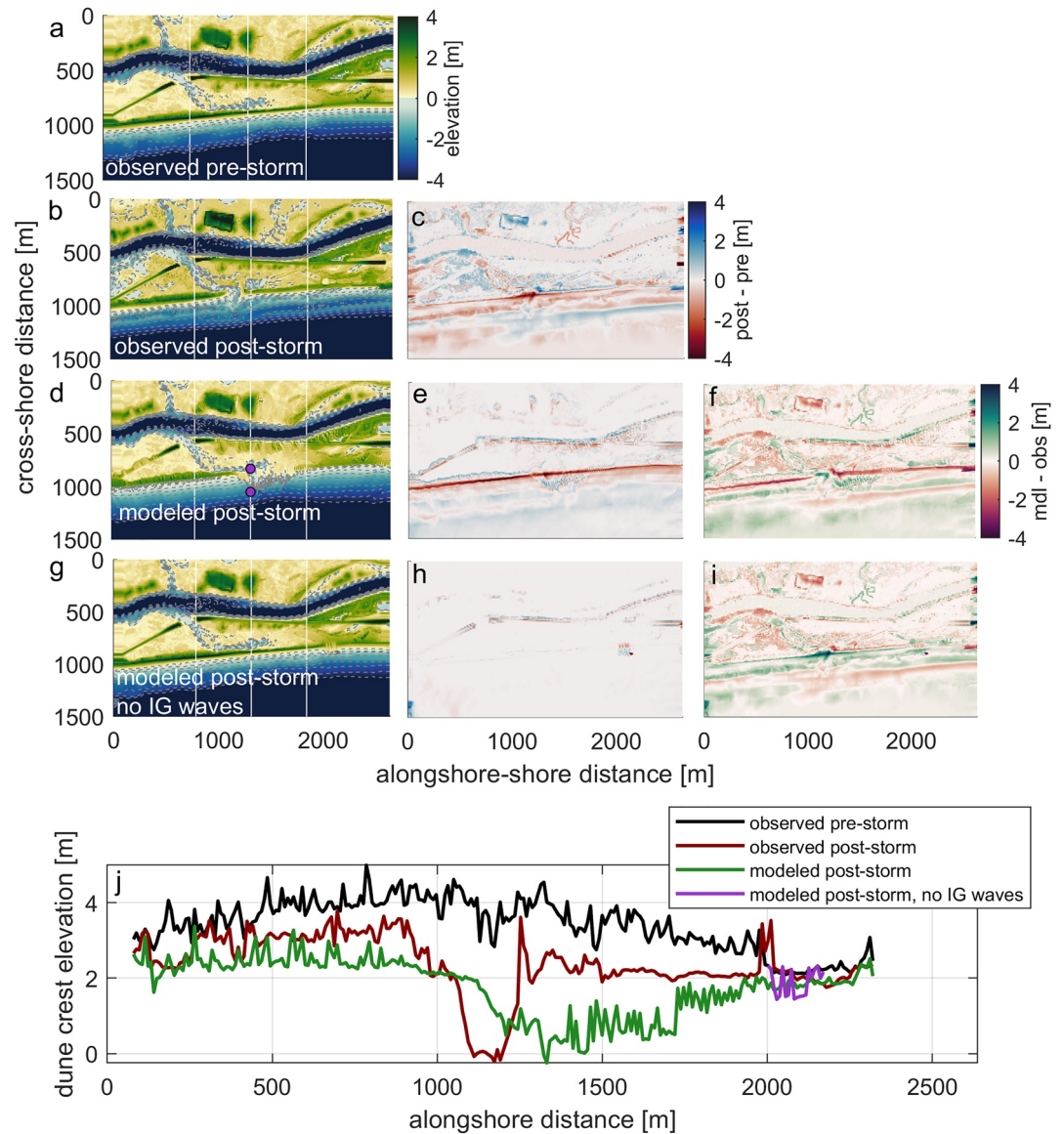


Figure 6. (a) Observed pre- and (b) post-storm and (d and g) modeled post-storm topography and bathymetry for Matanzas, FL after Hurricane Matthew. Contours indicate 0:4 m depth in 0.5 m increments. The two points in d indicate where water levels were extracted to calculate cross-barrier gradients. White lines indicate cross-barrier transects where hydro- and morphodynamics are further evaluated in Figure 9. (c) Observed and (e and h) modeled change during the storm. (f and i) Difference (modeled – observed) in change. (j) Pre- and post-storm observed and modeled dune crest elevations.

7. Matanzas Breach

7.1. Morphological Change

Before Hurricane Matthew, the barrier near the breach at Matanzas was characterized by continuous, high dunes exceeding 4 m toward the southern end and low dunes of ~2 m toward the northern end (Figures 6a and 6j). A shallow, lagoonal offshoot of the Intracoastal Waterway backed much of the barrier, though its connection to the Waterway had been modified by the US Army Corps of Engineers. Dune erosion and dune crest lowering (~1–2 m) were observed along the entire length of the barrier after Matthew (Figures 6b and 6c). Small washover deposits were also observed just landward of the dune crest along much of the southern and central sections of the barrier (Figure 6c). Sediment eroded from the beach face, dune face, and dune crest was deposited in a shore-parallel bar. A breach developed where the barrier island was backed by the lagoon (Figures 6b and 6c). Nearly 4 m of sediment was eroded at the breach location, with deposition evident in the nearshore.

Modeled morphological changes were characterized by widespread dune face and dune crest erosion and lowering (Figures 6d and 6e). Although the overall magnitude of erosion was overpredicted, modeled gradients in erosion magnitude from north to south matched observed gradients (Figure 6j). Deposition of sediment in washover fans, most notable along the southern extent of the barrier, and growth of the alongshore bar were well-represented. The model predicted a breach ~100 m north of the observed breach location and the elevation change associated with the breach matched observations. Modeled sediment eroded during breaching was deposited in the nearshore in a delta, as observed (Figure 6e). Overall patterns in differences between modeled and observed morphological change indicate that erosion of the dune crest was overpredicted in the model and that a large extent (~300 m) of the central part of the barrier was inundated (Figure 6j). Model skill for total bed level change was poor, with a BSS of 0.08. However, model skills for crest elevation, eroded volume, and deposited volume were reasonable to good, with BSSs of 0.38, 0.23, and 0.27, respectively.

7.2. Breaching Dynamics

The Matanzas breach developed uniquely, as elevated water levels in the Intracoastal Waterway and back-barrier lagoon ultimately breached the eroded barrier from the landward side. To analyze the hydrodynamics, we followed a similar model analysis as described for Fire Island. We sampled modeled water levels from a location in the back-barrier lagoon and from a location at 2 m depth in the nearshore along the cross-barrier transect through the breach (Figures 6d and 7a). The locations were separated by 70 m in the cross-shore. Negative gradients indicate that back-barrier water levels were higher than ocean water levels, driving flow toward the ocean (Figure 7b). To assess morphodynamics, at each of three cross-barrier transects (Figure 6), bedload sediment transport was separated into the onshore and offshore directions and was integrated in space over three profile zones: the nearshore, subaerial beach, and dune crest landward to the back-barrier (Figure 8). Suspended load transport was of equal magnitude to bedload transport in the nearshore, but nearly zero landward of the waterline. To quantify the importance of IG waves in breaching, we performed an additional model experiment in which we did not impose an incoming bound IG wave and suppressed IG wave generation and wave rollers within the model domain.

Model results suggest that incident wave heights were 2-m high at the beginning of the storm on 7 October 2016 at 0600 UTC, it was high tide in the ocean, and water levels in the back-barrier and in the nearshore were roughly equal at ~1 m so there was no cross-shore gradient (Figure 7). Predicted offshore-directed bedload transport along the entire barrier was associated with erosion of intertidal sediments and beach berms during the early stages of the collision regime, which accumulated in an alongshore bar (Figure 8). Due to a phase lag in the tide between the ocean and the back-barrier, which is 2 km south of the inlet where Intracoastal Waterway and ocean waters exchange, an offshore-directed (negative) water-level gradient began to develop immediately. As wind- and SLP-forced surge increased on the ocean side, those water-level anomalies propagated to the back-barrier via the Intracoastal Waterway.

As waves became larger, near 0800 UTC, modeled water levels in the nearshore became increasingly modulated by SS wave groups and IG waves (Figures 7a and 7c). At the northern transect, low initial dune heights resulted in overwash and subsequent erosion of the dune early in the event, from 0800 UTC to 1200 UTC (Figure 8a). Negative water level gradients rapidly increased in magnitude as incident wave heights reached 4–5 m after 1200 UTC due to substantial overwash at the northern transect, which transported sediment and water to the back-barrier (Figures 7d, 8a and 9a). Interestingly, offshore-directed bedload transport remained large despite episodic overwash. At the central and southern transects where dunes were higher, bedload transport continued to be offshore-directed due to dune erosion during collision, until these locations transitioned to the overwash regime when incident wave heights peaked. Though not shown, water level gradients at this time were substantial, but the dunes were not sufficiently lowered to enable flow.

Onshore-directed bedload transport during overwash became significant at ~1500 UTC at the breach transect, and ~1600 UTC at the southern transect when ocean water levels reached 2 m and incident wave heights reached 7 m (Figures 7, 8b, 8c, 9b, 9e and 9h). Fluxes of water into the back-barrier during overwash were evident in the back-barrier water level time series (Figure 7a). By ~1700 UTC, the barrier from the central to northern transect was inundated. Vertically resolved cross-shore currents indicate that flow was toward the back-barrier over the inundated barrier, and that wave-driven onshore surface currents and return flow at depth persisted seaward of the dune crest despite inundation (Figures 9b, 9e and 9h). Bedload transport in either direction was small along the

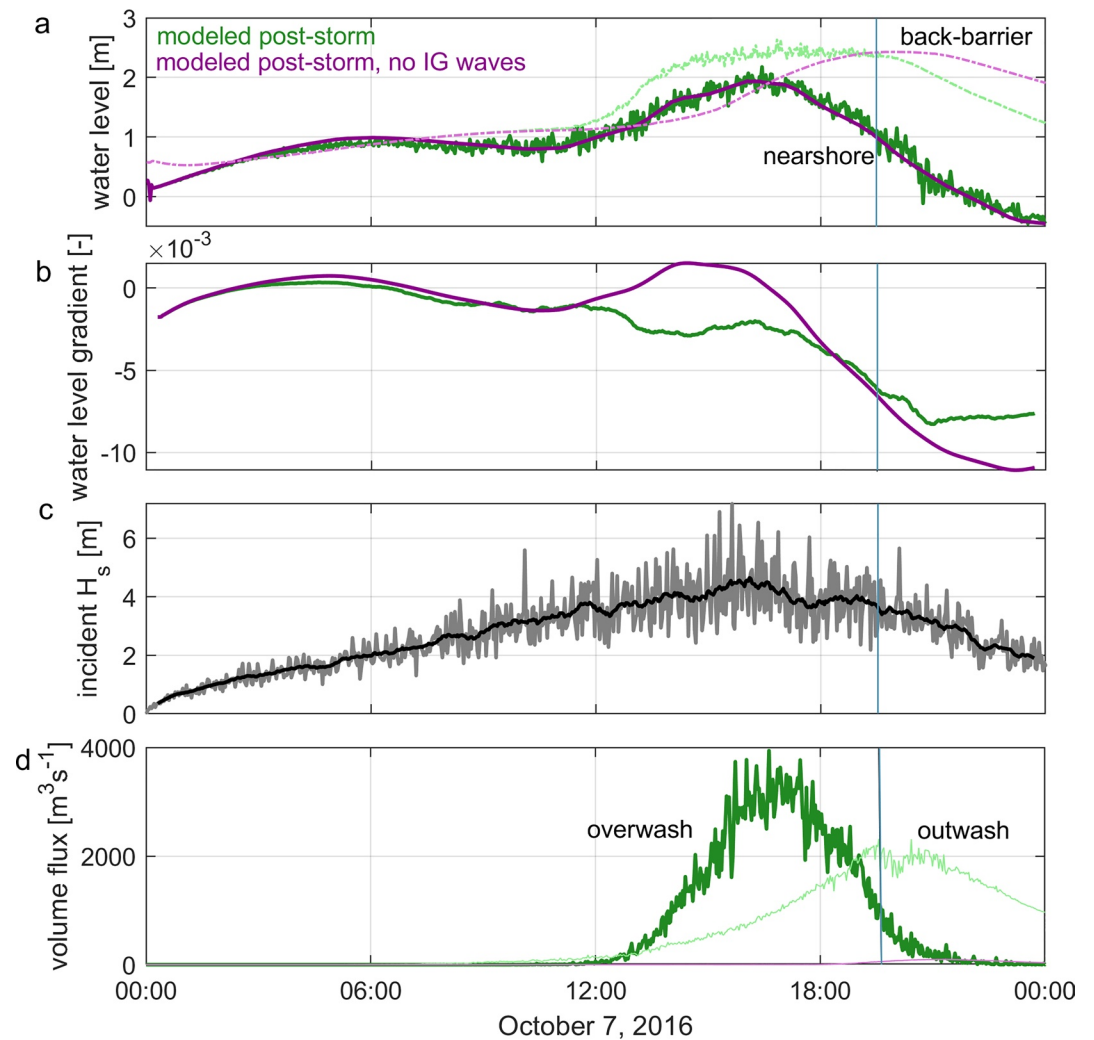


Figure 7. Time series of Hurricane Matthew (a) water levels in the nearshore (solid) and back-barrier (dashed) for the baseline model simulation and a simulation without infragravity waves. (b) The cross-barrier water level gradient, averaged over individual wave groups, where negative indicates an offshore-directed water level gradient, (c) Incident significant wave height (H_s) at the wave group scale (gray) and averaged (black), and (d) Onshore (thick lines) and offshore (thin lines) volume flux over the dune crest integrated in the alongshore. Blue vertical lines indicate the approximate time of breaching.

inundated barrier. At the southern transect, model results suggest that overwash remained the dominant mechanism for sediment transport and water fluxes (Figure 8c).

Recession of ocean water levels and decreasing incident wave energy accelerated the development of the negative water level gradient between the back-barrier and ocean (Figure 7). Inundation by ocean water levels receded and overwash became less frequent. By 1900 UTC, surface cross-barrier currents over the dune crest were ocean-directed, though small, and bedload transport was directed offshore. At this time, dune crests along the central and northern sections of the barrier island were predicted to have been lowered by ~ 3 and ~ 1.5 m, respectively. Further recession of ocean wave levels continued to build a pressure head over the vulnerable dune crest, until the model predicted breaching the back-barrier toward the ocean at 2000 UTC with 5 m/s currents, associated with offshore-directed bedload transport rates of nearly 300 kg/m/s that eroded the barrier island across the central transect (Figures 8b, 9c, 9f and 9i). Deposition of sediment in the nearshore occurred where the breaching currents met the nearshore environment.

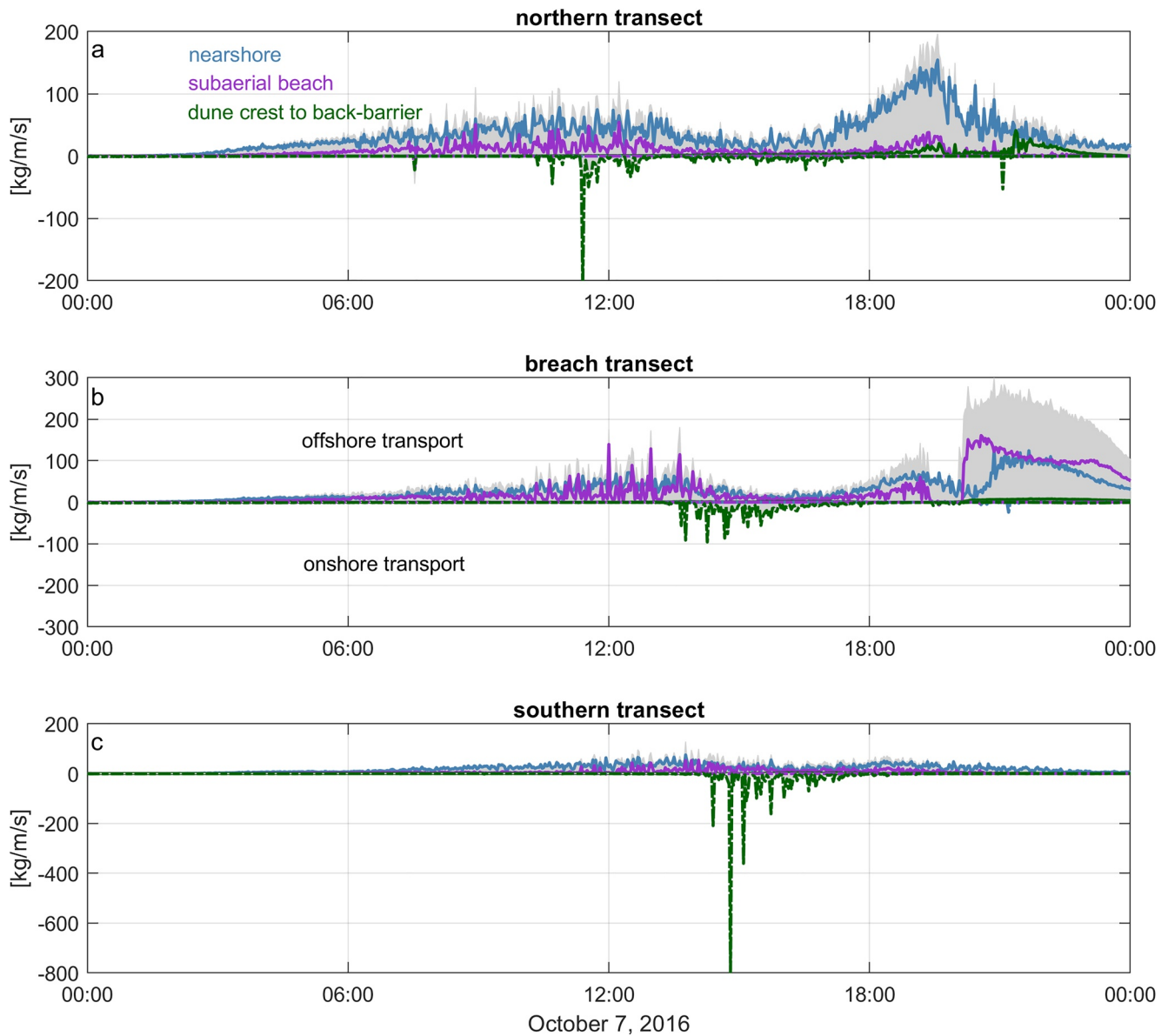


Figure 8. Time series of bedload sediment transport along three cross-barrier transects: (a) northern, (b) breach, and (c) southern (Figure 6). Transport in the onshore (negative) and offshore (positive) directions was spatially integrated over the nearshore (blue), subaerial beach (magenta), and dune crest landward to the back-barrier (green) for each transect. Onshore and offshore transport integrated over the entire transect is shaded in gray. *Note.* Limits on the ordinate differ for each subplot.

Though the ocean-directed water level gradient across the barrier ultimately formed the breach, IG waves were a dominant process leading to breaching. In the simulation without IG waves, the beach face and dune were nearly completely preserved, except for a small breach at the northern transect (Figure 6). Though nearshore water levels in this simulation were similar on average to those in the baseline simulation, back-barrier water levels were different, despite the same boundary conditions (Figure 7). Without IG waves, dune crests were not lowered and overwash did not occur. The lack of volume flux of water over the dune crest yielded lower back-barrier water levels, and a back-barrier directed water level gradient briefly formed at 1400 UTC. When the back-barrier surge reached its peak, a stronger gradient existed between the back-barrier and ocean because major breaching and outwash did not occur, and the low-lying dunes near the northern transect were weakly breached. The importance of oceanside processes during a back-barrier breaching event illustrates that the temporally varying co-evolution of the morphodynamics and hydrodynamics is critical to resolve.

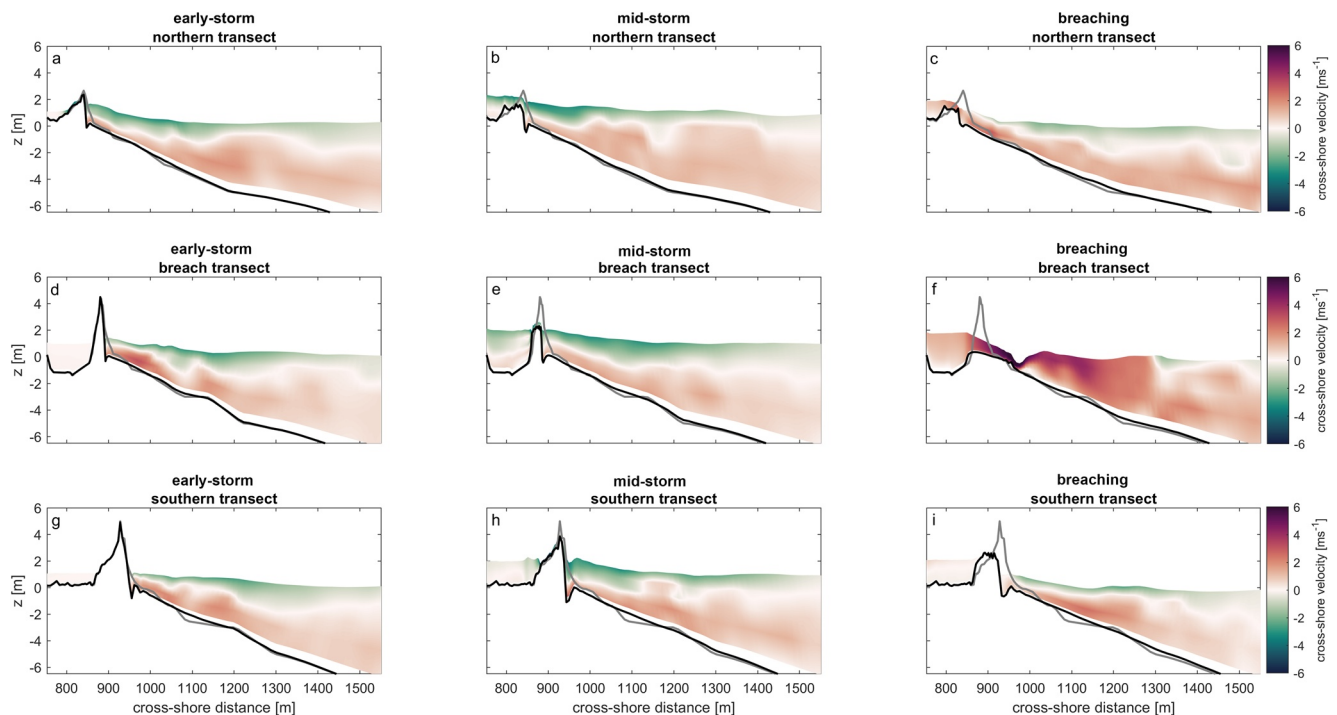


Figure 9. Cross-shore velocity at three instances in time—(a), (d), (g) early storm characterized by dune collision, (b), (e), (h) mid-storm characterized by episodic overwash, and (c), (f), (i) at the moment of breaching—along three cross-barrier transects: northern, breach, and southern (Figure 6). Onshore velocities are negative (green) and offshore velocities are positive (red). Black lines indicate profiles at the instance in time, whereas gray lines indicate the initial profile.

van der Lugt et al. (2019) analyzed the evolution of the Sallenger regimes for this location and event and similarly described alongshore differences in the morphological change. Overall, results found in this work are consistent with their analyses and model skill is comparable, despite differences in the forcing, model physics and parameterizations, and calibration. van der Lugt et al. (2019) explored sensitivity of the modeled morphological changes to uncertainty in the incident wave height, surge, and back-barrier water levels. Near the Matanzas breach, they found sensitivity to the offshore surge and to the back-barrier water levels; however, breaching occurred in all simulations. We argue that uncertainty in the magnitude of the IG waves, which can drive total water levels during extreme conditions, is another factor to consider.

8. Conclusions

Understanding of barrier island breaching has historically been limited by: (a) sparseness of in situ observations of hydro- and morphodynamics during extreme events, (b) cross-shore transect based frameworks for evaluating observed or modeled hydrodynamic processes, which ignore alongshore variations in hydro- and morphodynamics, and (c) 2D horizontal modeling approaches, which do not resolve the vertical structure of nearshore currents or sediment transport. In this work, we used a coupled ocean-wave-IG wave-sediment transport model to simulate hydrodynamic processes that drive barrier island morphological change over ocean basin to local spatial scales. Morphodynamics were simulated at the highest resolution (O [2 m]) at Fire Island, NY during Hurricane Sandy and at Matanzas, FL during Hurricane Matthew. Back-barrier breaching occurred at Matanzas, driven by highly localized hydrodynamics, including alongshore variations in wave overtopping and development of an ocean-directed water-level gradient across the barrier. Breaching at Fire Island was driven by elevated ocean water levels and wave attack and overwash.

Observed alongshore and cross-shore variations in morphological response were modeled with good skill and modeled breaches developed in locations nearby observed breaches at Fire Island and Matanzas, despite differences in the physical processes that caused change. At Matanzas, the breach was predicted 100 m north of the observed breach, and at Fire Island, the main breach was predicted 250 m west of the observed breach. Modeled morphological response tended to be larger than that observed at both locations. Morphological change

at Fire Island was sensitive to landcover effects, represented by the vegetation module of COAWST. Interestingly, morphological change was not sensitive to, or improved by inclusion of landcover characteristics by only modifying the bed roughness length, though this method has been demonstrated to be effective in XBeach-Surfbeat modeling (Passeri et al., 2018; van der Lugt, 2019). Modeled morphological changes were similar to modeled changes presented in van der Lugt et al. (2019), namely extensive back-barrier channelization and deposition, and breach locations. This may indicate that models do not properly represent controlling processes, such as lateral erosion, bed stratigraphy, and vegetation effects. Introduction of new models to represent physical processes can reveal gaps in knowledge, weakness of model physics and parameterizations, and different sensitivity to hydro- and morphodynamics. This work underscores the importance of resolving the complexity of nearshore and back-barrier systems when investigating or predicting barrier island breaching during extreme events.

Data Availability Statement

Model data can be found at <https://www.sciencebase.gov/catalog/item/609bf69ed34ea221ce39b261>. Figure colormaps are from Thyng et al. (2016).

Acknowledgments

C. A. Hegermiller is grateful to the U.S. Geological Survey (USGS) Mendenhall Research Fellowship Program for support. This project was supported by the USGS Coastal and Marine Geology Program and the Office of Naval Research, Increasing the Fidelity of Morphological Storm Impact Predictions Project. M. Olabarieta acknowledges support from the NSF project OCE-1554892. The authors thank Mark Buckley (USGS) and three anonymous reviewers whose discussions improved this work greatly.

References

- Baar, A. W., Boechat, A. M., Van Dijk, W. M., & Kleinans, M. G. (2019). Critical dependence of morphodynamic models of fluvial and tidal systems on empirical downslope sediment transport. *Nature Communications*, *10*, 4903.
- Beudin, A., Kalra, T. S., Ganju, N. K., & Warner, J. C. (2017). Development of a coupled wave-flow-vegetation interaction model. *Computers & Geosciences*, *100*, 76–86. <https://doi.org/10.1016/j.cageo.2016.12.010>
- Booij, N., Ris, R. C., & Holthuijsen, L. H. (1999). A third generation wave model for coastal regions, Part I. Modeling description and validation. *Journal of Geophysical Research*, *104*, 7649–7666. <https://doi.org/10.1029/98JC02622>
- Callaghan, D. P., Ranasinghe, R., & Roelvink, D. (2013). Probabilistic estimation of storm erosion using analytical, semi-empirical, and process based storm erosion models. *Coastal Engineering*, *82*, 64–75. <https://doi.org/10.1016/j.coastaleng.2013.08.007>
- Cañizares, R., & Irish, J. L. (2008). Simulation of storm-induced barrier island morphodynamics and flooding. *Coastal Engineering*, *55*, 1089–1101. <https://doi.org/10.1016/j.coastaleng.2008.04.006>
- Coogan, J., Webb, B., Smallegan, S., & Puleo, J. (2019). Geomorphic changes measured on Dauphin Island, AL, during Hurricane Nate. *Shore and Beach*, *87*(4), 8. <https://doi.org/10.34237/1008742>
- Davis, C., Wang, W., Chen, S. S., Chen, Y., Corbosiero, K., DeMaria, M., et al. (2008). Prediction of landfalling hurricanes with the advanced Hurricane WRF model. *Monthly Weather Review*, *136*, 1990–2005. <https://doi.org/10.1175/2007MWR2085.1>
- De Vet, P. L. M., McCall, R. T., Den Bieman, J. P., Stive, M. J. F., & Van Ormondt, M. (2015). Modelling dune erosion, overwash and breaching at Fire Island (NY) during Hurricane Sandy. *The Proceedings of the Coastal Sediments*. https://doi.org/10.1142/9789814689977_0006
- de Winter, R. C., Gongriep, F., & Ruessink, B. G. (2015). Observations and modeling of alongshore variability in dune erosion at Egmond aan Zee, the Netherlands. *Coastal Engineering*, *99*, 167–175. <https://doi.org/10.1016/j.coastaleng.2015.02.005>
- Defne, Z., Ganju, N. K., & Moriarty, J. M. (2019). Hydrodynamic and morphologic response of a back-barrier estuary to an extratropical storm. *Journal of Geophysical Research: Oceans*, *124*, 7700–7717. <https://doi.org/10.1029/2019JC015238>
- Donnelly, C., Kraus, N., & Larson, M. (2006). State of knowledge on measurement and modeling of coastal overwash. *Journal of Coastal Research*, *22*(4), 965–991. <https://doi.org/10.2112/04-0431.1>
- Doyle, J., Hodur, R., Chen, S., Jin, Y., Msokaitis, J., Wang, S., et al. (2014). Tropical cyclone prediction using COAMPS-TC. *Oceanography*, *27*, 104–115. <https://doi.org/10.5670/oceanog.2014.72>
- Elsayed, S. M., & Oumeraci, H. (2017). Effect of beach slope and grain-stabilization on coastal sediment transport: An attempt to overcome the erosion overestimation by XBeach. *Coastal Engineering*, *121*, 179–196. <https://doi.org/10.1016/j.coastaleng.2016.12.009>
- Engelstad, A., Ruessink, B. G., Wesselman, D., Hoekstra, P., Oost, A., & van der Veegt, M. (2017). Observations of waves and currents during barrier island inundation. *Journal of Geophysical Research: Oceans*, *122*, 3152–3169. <https://doi.org/10.1002/2016JC012545>
- Fairall, C. W., Bradley, E. F., Hare, J. E., Grachev, A. A., & Edson, J. B. (2003). Bulk parameterization of air-sea fluxes: Updates and verification for the COARE algorithm. *Journal of Climate*, *16*, 571–591. [https://doi.org/10.1175/1520-0442\(2003\)016<0571:bpoasf>2.0.co;2](https://doi.org/10.1175/1520-0442(2003)016<0571:bpoasf>2.0.co;2)
- Fairall, C. W., Bradley, E. F., Rogers, D. P., Edson, J. B., & Young, G. S. (1996). Bulk parameterization of air-sea fluxes in TOGA COARE. *Journal of Geophysical Research*, *101*, 3747–3767. <https://doi.org/10.1029/95JC03205>
- Fredericks, X., Hapke, C. J., & Lentz, E. E. (2016). Coastal topography – Fire Island. U.S. Geological Survey Data Release.
- Gharagozlou, A., Dietrich, J. C., Massey, T. C., Anderson, D. L., Gorski, J. F., & Overton, M. F. (2021). Formation of a barrier island breach and its contributions to lagoonal circulation. *Estuarine, Coastal and Shelf Science*. <https://doi.org/10.1016/j.ecss.2021.107593>
- Goff, J. A., Allison, M. A., & Gulick, S. P. S. (2010). Offshore transport of sediment during cyclonic storms: Hurricane Ike (2008), Texas Gulf coast, USA. *Geology*, *38*, 351–354. <https://doi.org/10.1130/G30632.1>
- Goff, J. A., Swartz, J. M., Gulick, S. P. S., Dawson, C. N., & de Alegria-Arzaburu, A. R. (2019). An outflow event on the left side of Hurricane Harvey: Erosion of barrier sand and seaward transport through Aransas Pass, Texas. *Geomorphology*, *334*, 44–57. <https://doi.org/10.1016/j.geomorph.2019.02.038>
- Haidvogel, D. B., Arango, H., Budgell, W. P., Cornuelle, B. D., Curchitser, E., Di Lorenzo, E., et al. (2008). Ocean forecasting in terrain-following coordinates: Formulation and skill assessment of the Regional Ocean Modeling System. *Journal of Computational Physics*, *227*, 3595–3624. <https://doi.org/10.1016/j.jcp.2007.06.016>
- Haidvogel, D. B., Arango, H. G., Hedstrom, K., Beckmann, A., Malanotte-Rizzoli, P., & Shchepetkin, A. F. (2000). Model evaluation experiments in the North Atlantic Basin: Simulations in nonlinear terrain-following coordinates. *Dynamics of Atmospheres and Oceans*, *32*, 239–281. [https://doi.org/10.1016/S0377-0265\(00\)00049-X](https://doi.org/10.1016/S0377-0265(00)00049-X)

- Hapke, C. J., Brenner, O., Hehre, R., & Reynolds, B. J. (2013). Coastal change from Hurricane Sandy and the 2012–13 winter storm season – Fire Island (Open-File Report 2013-1231, p. 37). U.S. Geological Survey.
- Harter, C., & Figlus, J. (2017). Numerical modeling of the morphodynamic response of a low-lying barrier island beach and foredune system inundated during Hurricane Ike using XBeach and CSHORE. *Coastal Engineering*, 120, 64–74. <https://doi.org/10.1016/j.coastaleng.2016.11.005>
- Hegermiller, C. A., Warner, J. C., Olabarrieta, M., & Sherwood, C. R. (2019). Wave–current interaction between Hurricane Matthew wave fields and the Gulf Stream. *Journal of Physical Oceanography*, 49, 2883–2900. <https://doi.org/10.1175/JPO-D-19-0124.1>
- JALBTCX. (2016). 2016 USACE NCMP Topobathy LiDAR: Florida East Coast. NOAA National Centers for Environmental Information. <https://www.fisheries.noaa.gov/inport/item/49722>
- JALBTCX. (2017). 2016 USACE Post-Matthew Topobathy LiDAR: Southeast Coast (VA, NC, SC, GA, and FL). NOAA National Centers for Environmental Information. <https://www.fisheries.noaa.gov/inport/item/49616>
- Kalligeris, N., Smit, P. B., Ludka, B. C., Guza, R. T., & Gallien, T. W. (2020). Calibration and assessment of process-based numerical models for beach profile evolution in southern California. *Coastal Engineering*, 158, 103650. <https://doi.org/10.1016/j.coastaleng.2020.103650>
- Kalra, T. S., Aretxabaleta, A., Seshadri, P., Ganju, N. K., & Beudin, A. (2017). Sensitivity analysis of a coupled hydrodynamic-vegetation model using the effectively subsampled quadratures method (ESQM v5.2). *Geoscientific Model Development*, 10, 4511–4523. <https://doi.org/10.5194/gmd-10-4511-2017>
- Kalra, T. S., Sherwood, C. R., Warner, J. C., Rafati, Y., & Hsu, T.-J. (2019). Investigating bedload transport under asymmetrical waves using a coupled ocean-wave model. *The Proceedings of the Coastal Sediments*. https://doi.org/10.1142/9789811204487_0052
- Kumar, N., Voulgaris, G., Warner, J. C., & Olabarrieta, M. (2012). Implementation of the vortex force formalism in the Coupled Ocean-Atmosphere-Wave-Sediment Transport (COAWST) modeling system for inner shelf and surf zone applications. *Ocean Modelling*, 47, 65–95. <https://doi.org/10.1016/j.ocemod.2012.01.003>
- Landsea, C. W., & Franklin, J. L. (2013). Atlantic Hurricane database uncertainty and presentation of a new database format. *Monthly Weather Review*, 141, 3576–3592. <https://doi.org/10.1175/MWR-D-12-00254.1>
- McCall, R. T., Van Thiel de Vries, J. S. M., Plant, N. G., Van Dongeren, A. R., Roelvink, J. A., Thompson, D. M., & Reniers, A. J. H. M. (2010). Two-dimensional time dependent hurricane overwash and erosion modeling at Santa Rosa Island. *Coastal Engineering*, 57, 668–683. <https://doi.org/10.1016/j.coastaleng.2010.02.006>
- McCallum, B. E., Wicklein, S. M., Reiser, R. G., Busciolano, R. J., Morrison, J., Verdi, R. J., et al. (2013). Monitoring storm tide and flooding from Hurricane Sandy along the Atlantic coast of the United States, October 2012 (USGS Open File Report 2013-1043). <https://doi.org/10.3133/ofr20131043>
- Miselis, J. L., Andrews, B. D., Nicholson, R. S., Defne, Z., Ganju, N. K., & Navoy, A. (2016). Evolution of mid-Atlantic coastal and back-barrier estuary environments in response to a Hurricane: Implications for barrier-estuary connectivity. *Estuaries and Coasts*, 39, 916–934. <https://doi.org/10.1007/s12237-015-0057-x>
- NAIP. (2018). NAIP (National Agricultural Imagery Program). Retrieved from <https://www.fsa.usda.gov/programs-and-services/aerial-photography/imagery-programs/naip-imagery/>
- Over, J. R., Brown, J. A., Sherwood, C. R., Hegermiller, C. A., Wernette, P. A., Ritchie, A. C., & Warrick, J. A. (2021). A survey of storm-induced seaward-transport features observed during the 2019 and 2020 hurricane seasons. *Shore and Beach*, 89(2), 31–40. <https://doi.org/10.34237/1008924>
- Passeri, D. L., Long, J. W., Plant, N. G., Bilskie, M. V., & Hagen, S. C. (2018). The influence of bed friction variability due to land cover on storm-driven barrier island morphodynamics. *Coastal Engineering*, 132, 82–94. <https://doi.org/10.1016/j.coastaleng.2017.11.005>
- Pringle, W. J., Gonzalez-Lopez, J., Joyce, B. R., Westerink, J. J., & Westhuysen, A. J. (2019). Baroclinic coupling improves depth-integrated modeling of coastal sea level variations around Puerto Rico and the U.S. Virgin Islands. *Journal of Geophysical Research: Oceans*, 124, 2196–2217. <https://doi.org/10.1029/2018JC014682>
- Rafati, Y., Hsu, T.-J., Elgar, S., Raubenheimer, B., Quataert, E., & van Dongeren, A. (2021). Modeling the hydrodynamics and morphodynamics of sandbar migration events. *Coastal Engineering*, 103885. <https://doi.org/10.1016/j.coastaleng.2021.103885>
- Reniers, A. J. H. M., Roelvink, J. A., & Thornton, E. B. (2004). Morphodynamic modeling of an embayed beach under wave group forcing. *Journal of Geophysical Research*, 109, C01030. <https://doi.org/10.1029/2002JC001586>
- Roelvink, D., Reniers, A., van Dongeren, A., van Thiel de Vries, J., McCall, R., & Lescinski, J. (2009). Modelling storm impacts on beaches, dunes and barrier islands. *Coastal Engineering*, 56, 1133–1152. <https://doi.org/10.1016/j.coastaleng.2009.08.006>
- Roelvink, J. A. (1993). Dissipation in random wave groups incident on a beach. *Coastal Engineering*, 19, 127–150. [https://doi.org/10.1016/0378-3839\(93\)90021-Y](https://doi.org/10.1016/0378-3839(93)90021-Y)
- Safak, I., Warner, J. C., & List, J. H. (2016). Barrier island breach evolution: Alongshore transport and bay-ocean pressure gradient interactions. *Journal of Geophysical Research: Oceans*, 121, 8720–8730. <https://doi.org/10.1002/2016JC012029>
- Sallenger, A. H. (2000). Storm impact scale for barrier islands. *Journal of Coastal Research*, 16(3), 890–895.
- Schweiger, C., Kaehler, C., Koldrack, N., & Schuettrumpf, H. (2020). Spatial and temporal evaluation of storm-induced erosion modelling based on a two-dimensional field case including an artificial unvegetated research dune. *Coastal Engineering*, 161, 103752. <https://doi.org/10.1016/j.coastaleng.2020.103752>
- Shchepetkin, A. F., & McWilliams, J. C. (2005). The Regional Ocean Modeling System (ROMS): A split-explicit, free-surface, topography-following-coordinates Ocean Model. *Ocean Modelling*, 9, 347–404. <https://doi.org/10.1016/j.ocemod.2004.08.002>
- Sherwood, C. R., Long, J. W., Dickhudt, P. J., Dalyander, P. S., Thompson, D. M., & Plant, N. G. (2014). Inundation of a barrier island (Chandeleur Islands, Louisiana, USA) during a hurricane: Observed water-level gradients and modeled seaward sand transport. *Journal of Geophysical Research: Earth Surface*, 119, 1498–1515. <https://doi.org/10.1002/2013JF003069>
- Sherwood, C. R., Van Dongeren, A., Doyle, J., Hegermiller, C. A., Hsu, T. J., Kalra, T. S., et al. (2021). Modeling the morphodynamics of coastal responses to extreme events: What shape are we in? *Annual Review of Marine Science*, 14, 457–492. <https://doi.org/10.1146/annurev-marine-032221-090215>
- Sherwood, C. R., Warrick, J. A., Hill, A. D., Ritchie, A. C., Andrews, B. D., & Plant, N. G. (2018). Rapid, remote assessment of Hurricane Matthew Impacts using four-dimensional structure-from-motion photogrammetry. *Journal of Coastal Research*, 34, 1303. <https://doi.org/10.2112/JCOASTRES-D-18-00016.1>
- Simmons, J. A., Splinter, K. D., Harley, M. D., & Turner, I. L. (2019). Calibration data requirements for modelling subaerial beach storm erosion. *Coastal Engineering*, 152, 103507. <https://doi.org/10.1016/j.coastaleng.2019.103507>
- Smallgan, S. M., & Irish, J. L. (2017). Barrier island morphological change by bay-side storm surge. *Journal of Waterway, Port, Coastal, and Ocean Engineering*, 143(5). [https://doi.org/10.1061/\(ASCE\)WW.1943-5460.0000413](https://doi.org/10.1061/(ASCE)WW.1943-5460.0000413)
- Smart, (2004). An improved flow resistance formula. In M. Greco, A. Carravetta, & R. Della Morte (Eds.), *River Flow 2004; Proceedings of the second International Conference on Fluvial Hydraulics*. <https://doi.org/10.1201/b16998-34>

- Splinter, K. D., & Palmsten, M. L. (2012). Modeling dune response to an east coast low. *Marine Geology*, 329–331, 46–57. <https://doi.org/10.1016/j.margeo.2012.09.005>
- Stockdon, H. F., Doran, K. J., Sopkin, K. L., Smith, K. E. L., & Fredericks, X. (2013). Coastal topography – Northeast Atlantic coast, post-Hurricane Sandy, 2012 (U.S Geological Survey Data Series). <https://doi.org/10.3133/ds765>
- Sutherland, J., Peet, A. H., & Soulsby, R. L. (2004). Evaluating the performance of morphological models. *Coastal Engineering*, 51, 917–939. <https://doi.org/10.1016/j.coastaleng.2004.07.015>
- Taylor, P. K., Yelland, M. J., Thiel de Vries, J. V., Dongeren, A. V., McCall, R., & Reniers, A. (2001). The dependence of the sea surface roughness on the height and steepness of the waves. *Journal of Physical Oceanography*, 31, 572–590. <https://doi.org/10.9753/jfocce.v32.sediment.49>
- Thiel de Vries, J. V., Dongeren, A. V., McCall, R., & Reniers, A. (2011). The effect of the longshore dimension on dune erosion. *International Conference on Coastal Engineering*, 1, 49. <https://doi.org/10.9753/jfocce.v32.sediment.49>
- Thyng, K. M., Greene, C. A., Hetland, R. D., Zimmerle, H. M., & DiMarco, S. F. (2016). True colors of oceanography: Guidelines for effective and accurate colormap selection. *Oceanography*, 29(3), 9–13. <https://doi.org/10.5670/oceanog.2016.66>
- Uchiyama, Y., McWilliams, J. C., & Shchepetkin, A. F. (2010). Wave–current interaction in an oceanic circulation model with a vortex force formalism: Application to the surf zone. *Ocean Modelling*, 34, 16–35. <https://doi.org/10.1016/j.ocemod.2010.04.002>
- van der A, D. A., Ribberink, J. S., van der Werf, J. J., O'Donoghue, T., Buijsrogge, R. H., & Kranenburg, W. M. (2013). Practical sand transport formula for non-breaking waves and currents. *Coastal Engineering*, 76, 26–42. <https://doi.org/10.1016/j.coastaleng.2013.01.007>
- van der Lugt, M. A., Quataert, E., van Dongeren, A., van Ormondt, M., & Sherwood, C. R. (2019). Morphodynamic modeling of the response of two barrier islands to Atlantic hurricane forcing. *Estuarine, Coastal and Shelf Science*, 229, 106404. <https://doi.org/10.1016/j.ecss.2019.106404>
- Van Dongeren, A., Reniers, A., Battjes, J., & Svendsen, I. (2003). Numerical modeling of infragravity wave response during DELILAH. *Journal of Geophysical Research*, 108, 3288. <https://doi.org/10.1029/2002JC001332>
- Van Ormondt, M., Nelson, T. R., Hapke, C. J., & Roelvink, D. (2020). Morphodynamic modelling of the Wilderness Breach, Fire Island, New York. Part I: Model set-up and validation. *Coastal Engineering*, 157. <https://doi.org/10.1016/j.coastaleng.2019.103621>
- Vousdoukas, M. I., Ferreira, Ó., Almeida, L. P., & Pacheco, A. (2012). Toward reliable storm-hazard forecasts: XBeach calibration and its potential application in an operational early-warning system. *Ocean Dynamics*, 62, 1001–1015. <https://doi.org/10.1007/s10236-012-0544-6>
- Warner, J. C., Armstrong, B., He, R., & Zambon, J. B. (2010). Development of a Coupled Ocean-Atmosphere-Wave-Sediment Transport (COAWST) modeling system. *Ocean Modelling*, 35, 230–244. <https://doi.org/10.1016/j.ocemod.2010.07.010>
- Warner, J. C., Ganju, N., Sherwood, C. R., Kalra, T., Aretxabaleta, A., & Olabarrieta, M. (2019). A Coupled-Ocean-Atmosphere-Wave-Sediment Transport numerical modeling system (COAWST). USGS GitHub Code Repository. <https://doi.org/10.5066/P9NQUAOW>
- Warner, J. C., Schwab, W. C., List, J. H., Safak, I., Liste, M., & Baldwin, W. (2017). Inner-shelf ocean dynamics and seafloor morphologic changes during Hurricane Sandy. *Continental Shelf Research*, 138, 1–18. <https://doi.org/10.1016/j.csr.2017.02.003>
- Warner, J. C., Sherwood, C. R., Signell, R. P., Harris, C. K., & Arango, H. G. (2008). Development of a three-dimensional, regional, coupled wave, current, and sediment-transport model. *Computers & Geosciences*, 34, 1284–1306. <https://doi.org/10.1016/j.cageo.2008.02.012>
- Zheng, L., Weisberg, R. H., Huang, Y., Luettich, R. A., Westerink, J. J., Kerr, P. C., et al. (2013). Implications from the comparisons between two- and three-dimensional model simulations of the Hurricane Ike storm surge. *Journal of Geophysical Research: Oceans*, 118, 3350–3369. <https://doi.org/10.1002/jgrc.20248>

References From the Supporting Information

- Hasselmann, K. (1962). On the non-linear energy transfer in a gravity-wave spectrum: I. General theory. *Journal of Fluid Mechanics*, 12, 481–500. <https://doi.org/10.1017/S0022112062000373>
- Herbers, T. H. C., Elgar, S., & Guza, R. T. (1994). Infragravity-frequency (0.005 – 0.05 Hz) motions on the shelf: I. Forced waves. *Journal of Physical Oceanography*, 24, 917–927. [https://doi.org/10.1175/1520-0485\(1994\)024<0917:IFHMOT>2.0.CO;2](https://doi.org/10.1175/1520-0485(1994)024<0917:IFHMOT>2.0.CO;2)